Cerebral oximetry performance testing with a 3D-printed vascular array phantom

ALI AFSHARI, PEJMAN GHASSEMI, JONATHAN LIN, MOLLY HALPRIN, JIANTING WANG, GONZALO MENDOZA, SANDY WEININGER, AND T. JOSHUA PFEFER[*]

Center for Devices and Radiological Health, U.S. Food and Drug Administration, 10903 New Hampshire Avenue, Silver Spring, Maryland 20993, USA
joshua.pfefer@fda.hhs.gov

Abstract: Cerebral oximetry based on near-infrared spectroscopy represents a unique noninvasive tool for real-time surgical monitoring, yet studies have shown a significant discrepancy in accuracy among commercial systems. Towards the establishment of a standardized method for performance testing, we have studied a solid phantom approach – based on a 3D-printed cerebrovascular module (CVM) incorporating an array of 148 cylindrical channels – that has several advantages over liquid phantoms. Development and characterization of a CVM prototype are described, including high-resolution imaging and spectrophotometry measurements. The CVM was filled with whole bovine blood tuned over an oxygen saturation range of 30-90% and molded-silicone layers simulating extracerebral tissues were used to evaluate penetration depth. Saturation measurement accuracy was assessed in two commercially-available clinical cerebral oximeters. For one oximeter, both neonatal and pediatric sensors showed a high degree of precision, whereas accuracy was strongly dependent on saturation level and extracerebral geometry. The second oximeter showed worse precision, yet greater robustness to variations in extracerebral layers. These results indicate that 3D-printed channel array phantoms represent a promising new approach for standardized testing of clinical oximeters.

1. Introduction

Tissue oximeters based on near-infrared spectroscopy (NIRS) have become increasingly common for cerebral oxygenation monitoring of premature infants in intensive care units [1,2], as well as during neonatal and pediatric surgeries, particularly cardiac procedures [3,4]. The ability of NIRS-based devices to assess cerebral oxygen saturation enables real-time intervention to mitigate ischemia–reperfusion events or defects in inherited metabolic pathways [5]. In adults, active cerebral monitoring with oximeters can have an important impact during and after cardiovascular surgery and neurosurgery [6]. Effective devices can reduce mortality, transfusion rates and resource consumption while mitigating the risk of side effects that can adversely impact neurodevelopment or cardiac function [7,8].

Despite broad clinical implementation of cerebral oximeters, research has raised several questions regarding the performance of these devices. Inconsistency among commercial systems is a primary issue. For instance, Dix *et al.* [9] compared measurements from three commercial oximeters in 55 infants and found differences of 10 to 15% in tissue oxygenation (StO_2) values. In a study of five commercial oximeters in adults, Bickler *et al.* [10] found mean bias – defined as a difference between cerebral oximeter readings and the manufacturer-specified weighted arterial (SaO_2) and jugular bulb (SvO_2) saturation – varied from 3 to 13%. A number of other clinical studies have found significant differences in performance amongst cerebral oximeters [11–13]. The lack of standardization in clinical outputs have led some to conclude that cerebral oximeters are ineffective for estimating absolute StO_2 and should be limited to trend monitoring [10].

Differences in performance likely stem from variations in design features such as illumination wavelengths, illumination-collection geometry, component specifications and data processing algorithms. Because these variables impact light-tissue interactions, the quality of detected signals, and how StO_2 is calculated from these signals, they may determine robustness to inter- and intra-patient variations in anatomy (e.g., thickness of skull and sub-arachnoid space) and physiology (e.g., hematocrit, tissue turbidity). While manufacturers incorporate approaches such as multiple source-detector separation distances and specialized algorithms to minimize interference from extracerebral tissues, differing implementations may lead to diverse outcomes [14,15]. Identifying an effective paradigm for benchtop evaluation that addresses biological factors known to impact performance would represent a major step toward satisfying the need for standardization that many researchers have advocated [13,16].

In vivo testing of cerebral oximeters in healthy human subjects is currently the dominant method for establishing performance; however, this approach has several significant limitations [17]: (a) a lack of a single "gold standard" reference value for StO_2, as NIRS devices sample arteries, veins and capillaries with a variety of saturation levels; (b) a lack of clear insight into whether devices are sensing the brain or more superficial tissues; (c) a reliance on the assumption that StO_2 measurements in the superficial frontal cortex are equivalent to a weighted mean of arterial and venous saturation levels [17] – which may not be accurate in a wide variety of subjects under a range of physiological conditions [18]; and (d) the fact that ethical considerations preclude healthy subject testing at low saturation or blood concentration levels, or in children and infants. Thus, other approaches may be appropriate for augmenting or replacing volunteer subject clinical trials for validation; such as clinical convenience sample studies [19] and benchtop test methods.

Performance testing based on tissue-simulating phantoms provides an alternate approach for generating evidence of device effectiveness, in a manner analogous to standardized image quality test methods for established medical imaging modalities like ultrasound [20]. Phantom-based performance tests for NIRS oximeters can provide a rigorous, reproducible and convenient approach to evaluating performance using well-characterized materials and gold standard referencing of oxygenation levels. Such methods enable well-controlled studies of a wide range of variables such as patient-to-patient variations in tissue morphology (e.g., skull thickness) and physiology (e.g., hematocrit, optical properties) or device design variables (e.g., illumination wavelengths, illumination-collection geometry). Such an approach has the potential to quantitatively elucidate differences in device performance characteristics and robustness to confounding biological factors [21]. In addition to device validation, phantom-based test methods can facilitate early device development, quality control for manufacturing and constancy testing in clinical settings.

Liquid phantoms based on commercial fat emulsions such as Intralipid are often used in NIRS performance testing, as they can be mixed with blood to achieve tissue-relevant optical properties [22,23]. Blood oxygen saturation has been modified to achieve a range of target levels by introduction of oxygen and nitrogen gas [24], or by adding reducing agents such as yeast [18] or sodium dithionite [25]. This type of phantom has been implemented to evaluate performance of cerebral oximeters. Earlier versions of Intralipid-based phantoms for tissue oximetry involved direct immersion of sensors in the liquid medium [26,27]. More recently, investigators have used Intralipid-blood solutions along with solid silicone layers to represent extra-cerebral [18] and superficial skin/fat tissues [28]. While liquid phantoms have provided useful insights into oximeter performance, they also have a number of inherent disadvantages. First, blood/hemoglobin-Intralipid phantoms have been shown to exhibit signal drift over a period of hours due to changes in lipids that affect scattering [29,30]. Second, referencing to StO_2 can pose challenges, as a gold standard approach like CO-oximetry may not be effective for dilute, turbid samples and diffuse-reflectance-based methods (e.g., frequency domain NIRS) may not be sufficiently accurate and/or can be expensive. Third, the development of a

specialized system for controlling and monitoring a turbid, blood-based liquid phantom – especially when a stable, non-equilibrium saturation level is desired – can be burdensome due to the specialized equipment, labor and knowledge required.

Solid polymer phantoms containing fluid channels filled with blood or hemoglobin solutions may represent an effective alternative for testing oximeters. Over 20 years ago, Kurth *et al.* [24] introduced a solid brain phantom for NIRS constructed from polyester resin mixed with TiO_2 and incorporating 500 blood-filled channels with a 0.5 mm inner diameter. While we are not aware of any subsequent studies implementing this type of high-density channel-array approach for NIRS, it may now be possible to generate similar phantoms with less effort and greater flexibility using 3D printing technology. Our lab has pioneered the fabrication of 3D-printed biophotonic phantoms [31], developing models with both idealized and biomimetic vascular geometries for evaluation of hyperspectral and fluorescence imaging systems [31–33]. Other groups have also shown success in developing 3D-printed phantoms for different biophotonic applications [34,35]. Channel array phantoms not only enable the use of CO-oximetry for referencing of blood samples but provide a matrix material that is stable during measurements and relatively easy to fabricate, handle, and measure. Furthermore, this approach enables rapid re-design and dissemination of new phantom geometries.

The purpose of this study was to evaluate the potential for improving phantom-based testing of NIRS oximeters using emerging 3D printing technology. Specifically, our goals were: (1) characterize optical properties and channel morphology for a promising printer/material combination; (2) generate a prototype cerebrovascular module (CVM) incorporating an array of blood-filled channels as part of a phantom with removable layers and demonstrate that it produces reasonable values when measured with commercial cerebral oximeters; and (3) perform a parametric evaluation of the impact of extracerebral layers on clinical cerebral oximeter performance. By establishing a proof-of-principle for 3D-printed oximetry phantoms, this work has the potential to provide a foundation for other advances in tissue phantoms for NIRS technology and lead to new standardized test methods.

2. Methods

2.1 Modular phantom overview

Phantoms were comprised of three primary components (Fig. 1): the 3D-printed CVM and two superficial layers based on a polydimethylsiloxane (PDMS) matrix – one simulating the skin/skull/scalp region (Layer 1) and a second simulating cerebrospinal fluid (CSF) in the subarachnoid space (Layer 2). The literature indicates thickness ranges for scalp, skull, and cerebrospinal fluid regions of 0.7 - 5.0 mm [36–38], 0.8 - 3.2 mm [37–39], and 0.7 - 6.1 mm [37,38,40], respectively. Therefore, four versions of Layer 1 were fabricated, with thicknesses (T_{L1}) of 1.0, 2.5, 5.0, and 7.5 mm; two versions of Layer 2 were fabricated, with thicknesses (T_{L2}) of 1.0 and 2.5 mm. The CVM was 3.25 cm thick.
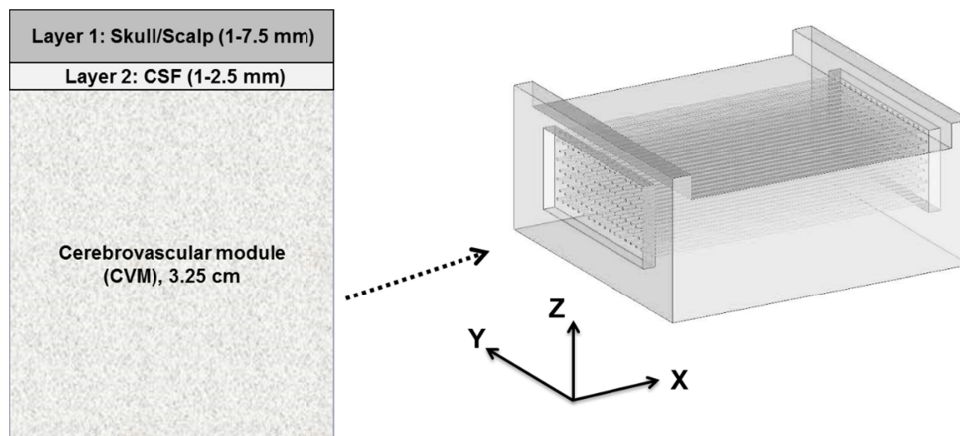
Fig. 1. Schematic of modular cerebral oximetry phantom (left) with layer thicknesses noted; right: Design of CVM from STL file used for 3D printing. Perfused channel-array region had dimensions of 120 x 80 x 32.5 mm.

2.2 CVM design and fabrication

To fabricate the CVM, we employed a triple-jetting 3D printer (Connex3 Objet260, Stratasys Ltd., Eden Prairie, MN, USA) based on UV-curing of photopolymers. This 3D-printer has the following nominal resolution: X-axis - 24 dots per millimeter (dpmm); Y-axis - 24 dpmm; and Z-axis - 63 dpmm and has an accuracy as small as 200 μm for full model size. Absorption and reduced scattering coefficients (μ_a and μ_s', respectively) measured in prior studies and displayed in Fig. 2 [41–45] were used to identify a proprietary photopolymer resin that was optically similar to neonatal cerebral tissue (VeroWhite, Stratasys). Optical properties of 3D-printed material samples (2 cm x 2 cm x 1 mm) were characterized using an integrating sphere spectrophotometer (Lambda 1050 UV/Vis/NIR, PerkinElmer, Inc., Waltham, MA, USA) and the inverse adding-doubling method [46]. Measurements of the proprietary resin selected show generally good agreement with the literature data. Figure 2(b) includes a curve for which the effect of 2.5% volume fraction of blood (total hemoglobin concentration of 54 μM, hematocrit of 49%) with StO_2 of 80% was added analytically to the measured μ_a of VeroWhite resin.
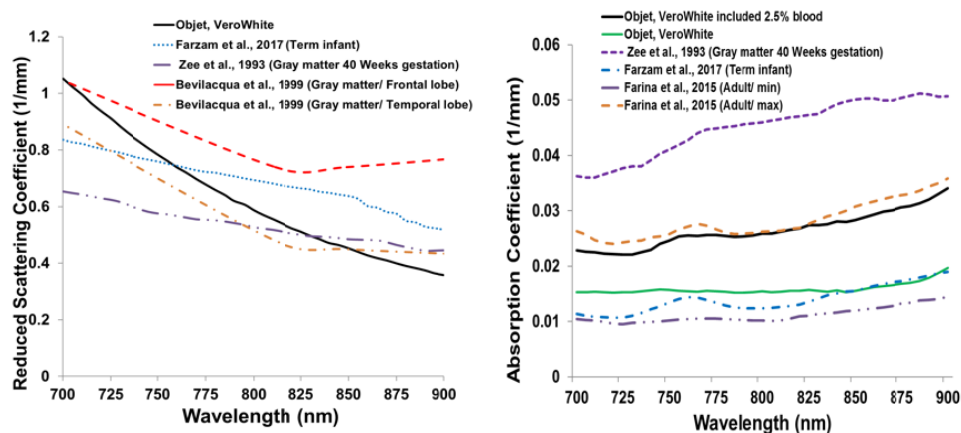

Fig. 2. (a) Reduced scattering and (b) absorption spectra of cured resin used to form channel-array modules, along with tissue optical property data from the literature (dashed lines).

We used a μCT imager (Scanco Medical μCT 100, Scanco USA Inc. Wayne, PA, USA) to assess phantom morphology. While the full CVM was too large to image, a single-layer

multi-channel array sample was printed and evaluated. Imaging results are presented in Fig. 3 along with a photograph of the sample with channels filled with India ink (Super black, Speedball Art product, Statesville, NC, USA). Imaging with microCT provides visualization of phantom nonuniformities or defects as well as quantification of printed feature sizes for comparison against designed geometry. Samples showed a homogeneous build, as opposed to the internal lattice structure we have seen with a fused deposition modeling printer [31]. Additionally, we evaluated the viability of channels over a range of diameters and identify the smallest useable size. As seen in Fig. 3, channels with nominal diameters greater than 0.6 mm are patent. Cross-sectional images of each channel were evaluated in four different locations along their length. The measured diameter was consistently smaller than the nominal value by approximately 0.1 mm, possibly due to flow of the liquid photopolymer during the solidification process.
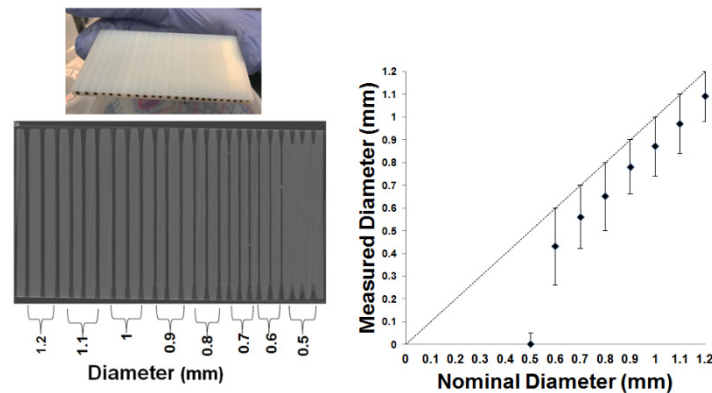

Fig. 3. Evaluation of 3D-printed test sample: (top left) photo of sample with ink-filled channels; (bottom left) μCT image of sample showing blockages in smaller channels, and (right) comparison of nominal vs. actual channel diameters, with blocked channels assigned a 0 mm diameter.

The CVM was constructed with overall dimensions of 130 x 120 x 50 mm, with the perfused channel-array region limited to a volume of 120 x 80 x 32.5 mm. Channel density was based in part on the total hemoglobin concentration (ctHb) of the neonatal brain, which the literature indicates is between 25 and 115 μM [18,37,47]. The CVM incorporated a total of 148 cylindrical linear channels spaced 4 mm apart in the vertical and horizontal directions, with the top row of channels (top edge) 0.8 mm below the phantom surface. Each channel had a nominal diameter of 0.90 mm, yet the mean measured channel diameter, based on μCT images of the thin multi-channel sample was 0.78 ± 0.12 mm (mean $\pm$ standard deviation). We also estimated the mean volume of the phantom channels by injecting water into the CVM and subtracting the volume of the side window regions, as well as by injecting known volumes of water directly into randomly selected individual channels (n = 8) until they were filled. The measured ctHb and channel diameter were 54 ± 0.08 μM and 0.75 ± 0.01 mm for the bulk water measurements; and 53 ± 0.06 μM and 0.74 ± 0.05 mm for the individual channel method. Two 3D-printed lids made of clear resin (120 x 55 x 60 mm) were also attached at the sides of the CVM by screws to minimize air exposure and subsequent reoxygenation of blood. Each lid contained a port (Fig. 2), which was used to attach a blood-filled syringe to one side and release air from the other. The impact of any boundary effects was investigated by comparing results obtained when the bottom and sides were covered either by aluminum foil or a black cloth. This was performed for two StO_2 levels with two different superficial layer cases ($T_{L1} = 0$, 7.5 mm). No significant difference in StO_2 was observed between these two cases, indicating that the phantom was sufficiently large as to produce negligible boundary effects.

2.3 Fabrication of Superficial Phantom Layers

To evaluate the impact of extra-cerebral layers on cerebral oximeter accuracy, we fabricated phantom layers to mimic scalp/skull and cerebrospinal fluid (CSF) regions. Figure 4 provides data on optical properties reported in the literature [18,45,48] used as approximate target values for these phantom layers. CSF in the subarachnoid space was modeled as a low-turbidity medium due to the influence of the arachnoid trabeculae [40]. Optical properties for this layer were previously estimated to be $\mu_a = 0.004$ mm^{-1} and $\mu'_s = 0.25$ mm^{-1} at $\lambda = 800$ nm (39). Scalp/skull layers were molded from 30 g PDMS (Sylgard 184 Silicone Elastomer, Dow Corning Corp., Washington, DC, USA) mixed with 0.28 g titanium dioxide (TiO$_2$, anatase titanium (IV) oxide, Sigma-Aldrich, St. Louis, MO, USA) and 0.01 g India ink. CSF layers were comprised of 30 g PDMS and 0.19 g TiO$_2$. PDMS solutions were mixed using a homogenizer (Tissue-Tearor, Model 985370, BioSpec Products Inc., Bartlesville, OK, USA) and the curing agent (Sylgard 184, Dow Corning) was added at a 10:1 ratio of silicone to curing agent, stirred, and then degassed using a vacuum chamber for half an hour (Labfirst Scientific and Industrial Equipment LLC, Cheyenne, WY, USA). After air bubbles were removed, the uncured materials were poured into Teflon molds to produce layers of 1 mm and 2.5 mm thickness. Samples were then cured in an oven for 3-4 hours at 75 °C.

An electronic height gauge device was used to validate PDMS layer thickness (Mitutoyo America Corp., series 570, Aurora, IL, USA), and all samples showed deviation less than 20% from the targeted thickness. PDMS layer optical properties were measured using an integrating sphere spectrophotometer, as described above. Resultant absorption and reduced scattering data for the scalp/skull and CSF layers were in good agreement with the literature [18,40,45,48].
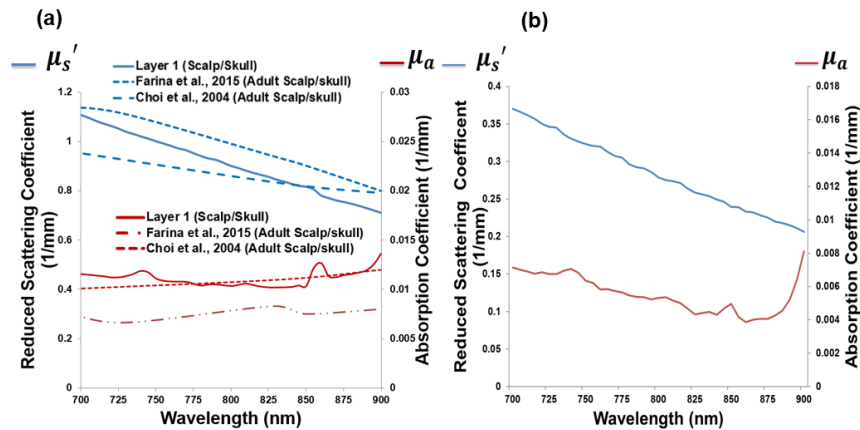

Fig. 4. Optical properties of (a) scalp/skull and (b) cerebrospinal fluid (CSF) simulating layers. Scalp/skull values are graphed with relevant tissue optical property data from the literature.
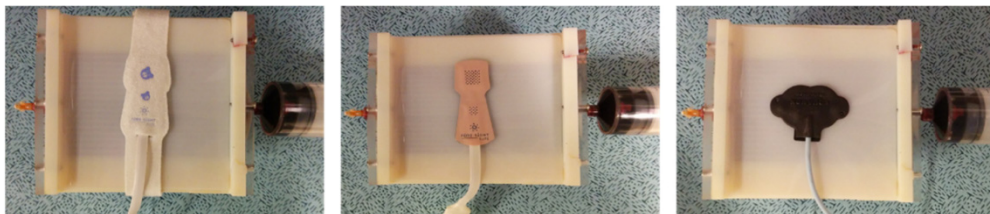

Fig. 5. Photos of the CVM) with 1 mm scalp/skull layer, NIRS probe placed on the top of channel area regarding Oximeter A - neo (left), Oximeter A - ped (center) and Oximeter B (right)

2.4 StO$_2$ level control

Measured extinction spectra of bovine oxyhemoglobin and deoxyhemoglobin samples showed negligible differences compared to those for human hemoglobin as reported previously [49]. Desaturation of stock, fully-oxygenated bovine blood samples (defibrinated whole blood, Quad Five, Ryegate, MT, USA) was performed using sodium dithionite (sodium hydrosulfite, Na$_2$S$_2$O$_4$, technical grade 85%, Sigma-Aldrich). Measurements with a whole-blood CO-oximeter (Avoximeter 4000, Accriva Diagnostic, Instrumentation Laboratory, Bedford, MA, USA) showed a consistent relationship between sodium dithionite concentration and StO$_2$ level (Fig. 6). Desaturation to steady state level occurred within 3 minutes after mixing. Repeated addition of sodium dithionite to blood samples can result in the production of methemoglobin (metHb), which has the potential to adversely influence StO$_2$ measurements given its spectral similarity to oxyhemoglobin but greater absorption coefficient values [50]. Regular monitoring of metHb level with a CO-oximeter was performed to ensure that the concentration of metHb remained less than 6% to avoid StO$_2$ estimation errors.
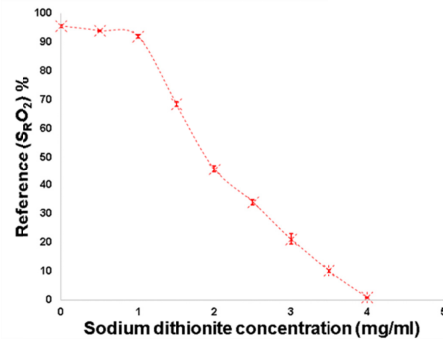

Fig. 6. Relationship between sodium dithionite concentration and StO$_2$ level measured by CO-oximeter.

2.5 Testing protocol

Two commercially available NIRS oximeters were used: Oximeter A, a Fore-Sight Elite (CAS Medical Systems, Inc., Branford, CT, USA) and Oximeter B, a SenSmart X-100 (Nonin Medical, Inc., Plymouth, MN). Oximeter A uses five wavelengths: 690, 730, 770, 810, and 870 nm. Two types of sensors were studied, each of which has one source and two detectors. The small (patients < 8 kg) – or neonatal – cerebral sensor had source-detector separation distances (SDs) of 9 and 25 mm; whereas the medium (patients > 3 kg) – or pediatric – cerebral sensor had SDs of 25 and 40 mm. Oximeter B uses four wavelengths: 730, 760, 810, 880 nm. We performed measurements with one sensor (patients < 40 kg), which had two sources and two detectors with SDs of 12.5 and 25 mm. For brevity, we will use the labels "Oximeter A – neo" and "Oximeter A – ped" to refer to the two Oximeter A sensors used.

Measurements of the final modular phantom (Fig. 5) were performed across a reference oxygen saturation (S$_R$O$_2$) range of 30-90%. The experimental procedure can be summarized in the following steps: (a) mixing pre-determined levels of sodium dithionite with bovine blood to achieve approximate StO$_2$ values, (b) recording reference S$_R$O$_2$ values from the CO-oximeter (which was repeated after cerebral oximeter measurements, using blood extracted from phantom), (c) inject blood mixture into the CVM using a 60 ml disposable syringe and allow 30 seconds before each measurement for sensor readings to become stable and (d) perform one measurement in each of three iterations (perpendicular, parallel and diagonal – approximately 45° – to the channels so as to ensure no effect of orientation). Sensor orientation was found to not be statistically significant both within these measurements as

well as in a separate set of measurements involving six data points in each orientation with each sensor. On average, S_RO_2 increased by $3.5 \pm 2.3\%$ over the course of each set of measurements, so mean S_RO_2 values were used in our analyses. Each saturation level measurement was performed using a fresh blood sample to avoid metHb formation during deoxygenation.

Paired cerebral and CO-oximeter data were processed using a number of metrics, most importantly, accuracy based on root-mean-square error (A_{rms}) and precision (S_{res}). Additionally, the slope of simple linear regression between measured and reference values was used to represent system sensitivity. The formulas used for computing A_{rms} and S_{res} are as follows:

$$A_{rms} = \sqrt{\frac{\sum_{i=1}^{n}(StO_{2i} - S_RO_{2i})^2}{n}}, \qquad (1)$$

$$s_{res} = \sqrt{\frac{\sum_{i=1}^{n}(StO_{2i} - StO_{2,fit,i})^2}{(n-2)}}, \qquad (2)$$

where StO_{2i} represents the mean oximeter measurement at the ith saturation level, S_RO_{2i} indicates the corresponding reference value, and n is the number of StO_2 levels in the measurement set. $StO_{2,fit,i}$ is the value of the fitted curve at the ith reference value. A_{rms} has been used in a pulse oximetry standard [51] to quantitate accuracy with respect to the reference measurement and is preferred over mean bias. The latter metric averages positive and negative local bias values that may cancel out, thus overestimating accuracy. S_{res} is based on deviation from a fit of measured results, so as to evaluate measurement variation rather than deviation from the reference.

3. Results

While quantitative analysis of data is critical to evaluate performance, our initial measurements involved the use of near-infrared imaging to elucidate the propagation of light emitted by the oximeters. We used a mobile phone camera (Android Nexus 5) with the NIR blocking filter removed (Eigen Imaging, Inc., San Diego, CA, USA). The images in Fig. 7 illustrate the output of Oximeter A's single source location and the overlapping exposure regions from the two source locations of the Oximeter B sensor.

Fig. 7. NIR images of sensors for Oximeters A - neo (left), A- ped (center) and Oximeter B (right) in use on the top surface of the phantom.

Performance testing results for the three cerebral oximeter sensors are presented in Figs. 8-10. Oximeter A - neo sensor data (Fig. 8) indicated that in almost all cases, the greatest error was produced at lower saturation levels, with data points for StO_2 values of 70% or greater showing minimal deviation with superficial layer thickness. The best accuracy was obtained for very minimal superficial layers and high StO_2 values. Increasing superficial layer thickness caused a monotonic decrease in both accuracy and sensitivity (defined, per Kleiser

et al. [18], from the slope of the curve). A_{rms} results increased monotonically from 5% to 21% as Layer 1 was increased from 0 to 7.5 mm. The T_{L2} = 2.5 mm case indicates a nearly complete loss of sensitivity to changes in StO$_2$.

Results for the Oximeter A - ped sensor (Fig. 9) were very similar to those for the neonatal sensor, except that for the T_{L1} = 1 mm series, three low readings at high saturation levels resulted in greater A_{rms} for this case than expected. It is also worth noting that results for the T_{L1} = 2.5 mm case showed slightly greater sensitivity than the Oximeter A - neo sensor did, which may indicate that the medium sensor was designed to address larger superficial layers.
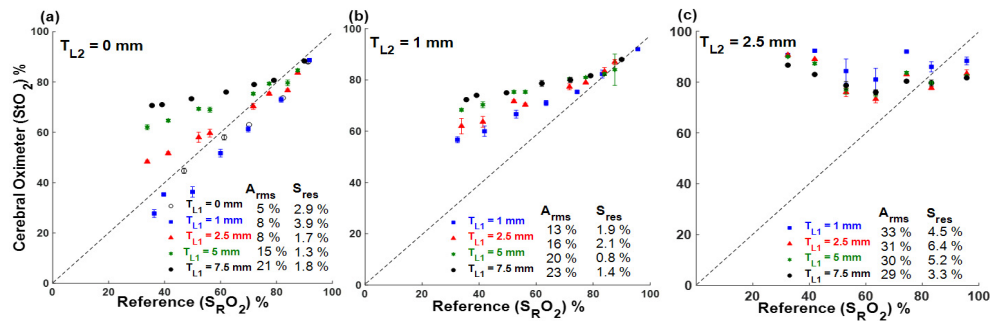

Fig. 8. Results from Oximeter A - neo for (a) T_{L2} = 0 mm (no CSF layer), (b) T_{L2} = 1 mm and (c) T_{L2} = 2.5 mm. Variables T_{L1} and T_{L2} represent scalp/skull and CSF layer thickness, respectively. Note that in the CVM, the first row of channels is 0.8 mm below the module surface. Error bars denote one standard deviation.
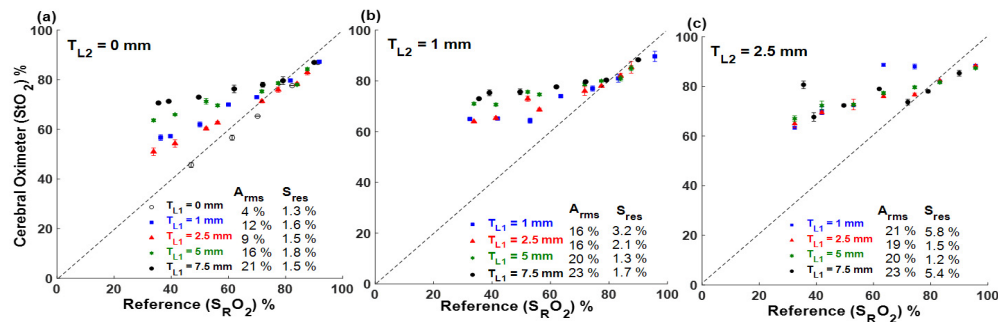

Fig. 9. Results from Oximeter A pediatric sensor for (a) T_{L2} = 0 mm, (b) T_{L2} = 1 mm, and (c) T_{L2} = 2.5 mm, where T_{L1} and T_{L2} represent scalp/skull and CSF layer thickness, respectively. Error bars denote one standard deviation.

Fig. 10. Results from Oximeter B neonatal sensor for (a) T_{L2} = 0 mm, (b) T_{L2} = 1 mm and (c) T_{L2} = 2.5 mm, where T_{L1} and T_{L2} represent scalp/skull and CSF layer thickness, respectively. Error bars denote one standard deviation.
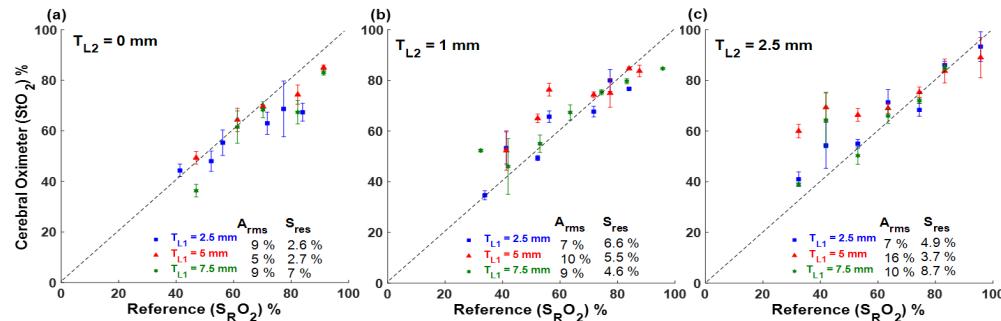
Results for the Oximeter B neonatal sensor (Fig. 10) were markedly different than those for Oximeter A with either small or medium sensors. Oximeter B showed worse precision than Oximeter A (about 2-3 times larger), which may have obscured trends due to layer thickness. Yet increasing T_{L1} or T_{L2} had comparatively minor impact on slope/sensitivity and bias. The $T_{L2} = 2.5$ mm case, which produced very poor sensitivity for Oximeter A, produced somewhat increased bias for Oximeter B, but there was minimal impact on slope and any trends due to T_{L1} were not clear.

To better understand the results provided for larger superficial layer thicknesses, we also fabricated a 4-cm-thick slab of scalp/skull-mimicking material – representing the limiting case – and measured it with each sensor and device. Oximeter A - neo and -ped sensors provided a mean StO_2 of 82.9 $\pm$ 1.4% and 74.9 $\pm$ 1.0%, respectively, whereas Oximeter B with a neonatal sensor provided a mean StO_2 of 99.9 $\pm$ 0.4%. It is also worth noting that a prior study [28] measured a superficial-tissue-mimicking slab with slightly different properties ($\mu_a = 0.059$ cm^{-1}, $\mu_s' = 5$ cm^{-1} at 692 nm) using the adult sensor of Oximeter B, and found a value of 78%; using the same sensor and our phantom slab, we measured an StO_2 of 73%.

4. Discussion

The modular, 3D-printed phantom approach developed and tested in this study has the potential to facilitate evaluation and inter-comparison of NIRS-based cerebral oximeters, including patient-specific factors that impact performance. In this section, we address three main issues: (1) evaluation of the validity of our phantom-based test method through comparisons with the literature, (2) insights provided by our results into the confounding effect of extra-cerebral tissue layers and (3) considerations of 3D-printed phantom quality.

4.1 Comparisons with liquid phantom studies

One approach to evaluating the suitability of our test method involved comparisons to prior studies implementing a more well-established liquid phantom [18,28,29]. In two of these articles, measurements were performed with a 2.5 mm-thick turbid silicone layer representing extra-cerebral tissues above mixtures of erythrocytes and Intralipid. Comparisons of test results are provided for both oximeters in Fig. 11. While these prior studies have not provided measured μ_a spectra for liquid phantoms, based on their composition, we estimate that their μ_a values are in the lower end of the range presented in the literature for cerebral tissue, whereas our CVM prototype is closer to the higher end of this range. We compared results for the Oximeter A - neo sensor as tested with our solid phantom and $T_{L1} = 2.5$ mm, $T_{L2} = 0$ mm, to prior results from a liquid phantom with ctHb = 47.5 and 75 μM a similar superficial layer [29]. These two data sets have a variety of features in common, including large positive bias at low-to-moderate StO_2 levels and a small amount of negative bias at high StO_2 levels. The liquid phantom measurements showed a linear regression slope of 0.49, whereas for our solid phantom a value of 0.63 was found. Although no A_{rms} data was provided in the prior study, based on published graphical data we approximate a value of 16.2% (interpolated for 54 μM). Our solid phantom measurements produced A_{rms} values of 7.5% and 8.9% for Oximeter A - neo and ped sensors, respectively. Overall, liquid and solid phantoms provided similar trends, with a minor to moderate level of discrepancy in quantitative values.

Measurements using Oximeter B and our solid phantom with $T_{L1} = 2.5$ mm, $T_{L2} = 0$ mm were compared with liquid phantom data for ctHb values of 45 and 70 μM Fig. 10(b) (19). While liquid phantom results were qualitatively similar to our Oximeter A data – with a large positive bias at low-to-moderate StO_2 levels and a small degree of negative bias at high StO_2 levels – our solid phantom results for Oximeter B showed less bias at high and low StO_2 values, but greater variability (worse precision). The sensitivity of liquid phantom measurements showed linear regression slopes of 0.41 (for ctHb = 45 μM) and 0.54 (for ctHb = 70 μM) (19), whereas our results indicated a slope closer to unity (0.6). Although no A_{rms}

data was provided for liquid phantoms, our estimate based on published graphical data is 15.5%. Our solid phantom measurements indicated a greater level of accuracy, with an A_{rms} of 9%. The source of this discrepancy between liquid and solid phantom results for Oximeter B remains unclear. While the source of the variability in Oximeter B data is also not known, our findings are consistent with a prior study which found same-site reproducibility for this device to be 4.6% vs. 2.9% for Oximeter A [52].
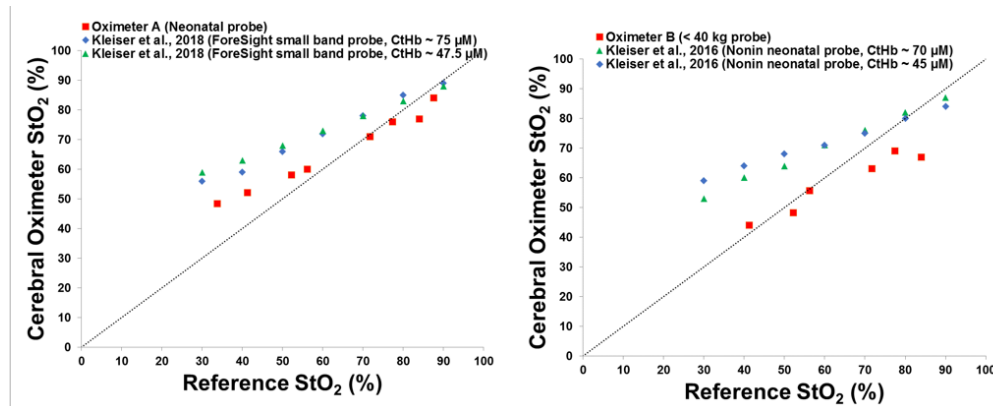

Fig. 11. Comparison of our solid phantom measurements with selected data from a prior liquid phantom study (19, 28). ctHb in our channel array phantom was 54 µM and in the cited research were (a) 47.5 and 75 µM and (b) 45 and 70 µM. Superficial layer thickness for all measurements was 2.5 mm.

Several clinical studies have demonstrated a lack of agreement between commercial cerebral oximeters however, little data was found in the literature on accuracy in neonates and children for the two devices studied. Schneider *et al.* [53] performed a clinical study of neonates which compared the two devices in the current study. Results showed relatively little difference, with StO_2 of 73.3%/74.2% (left/right hemisphere) for Oximeter A vs. 76.6%/77.8% for Oximeter B. These results agree with our findings that at high StO_2 values, relatively little difference in accuracy was seen between Oximeter A and B. Additionally, a clinical study of neonates by Hessel *et al.* [54] indicated that the Oximeter A neonate sensor produced a positive bias relative to a neonatal INVOS sensor at low saturations and negative bias at high saturations. Given that a neonatal INVOS sensor was shown by Kleiser *et al.* [29] to exhibit a consistent positive bias of 10-20%, but a nearly optimal sensitivity (slope close to 1.0), the results from Hessel *et al.* [54] are in qualitative agreement with our findings. It is also worth noting that in results with our phantom and the aforementioned liquid phantom [29], local bias tended to be greatest at StO_2 values of 40% or less. This would seem to indicate that the poorest performance occurs in an StO_2 range most relevant to unhealthy patients. Such an outcome may be attributable to the fact that safety concerns limit the range of StO_2 values over which clinical testing of cerebral oximeters can be performed in healthy human subjects [10].

4.2 Impact of extra-cerebral layers

Numerous prior studies have concluded that cerebral oximeter readings are influenced by extra-cerebral layers [14,55,56]. Our phantom-based test results provide insights into the quantitative impact of superficial layers on device performance. As layers simulating the scalp and skull and CSF-filled subarachnoid space were increased in thickness, there was a major increase in positive bias for Oximeter A neonatal sensor, with A_{rms} increasing from 5% for no superficial layers to 21% for $T_{L1} = 7.5$ mm, $T_{L2} = 1$ mm. When a CSF-simulating layer was present, the turbid layers showed much less sensitivity to changes in S_RO_2. Oximeter B shows less variation to changes in layer thickness. While the change in sensitivity/slope with

thickness is minimal for Oximeter B, minor degradation in accuracy and precision are apparent.

Some of this discrepancy in sensitivity to superficial layers between devices may be attributable to differences in sensor reflectivity. The tissue-contacting surface of Oximeter B appears black; however, the Oximeter A probes are light in color. Spectrophotometry indicated that the diffuse reflectance of both Oximeter A probes was approximately 58% at 800 nm, whereas the Oximeter B probe showed a value of about 5%; all three probes showed minimal variation across the 700-900 nm range. Highly absorbing sensor surfaces should minimize the re-entry of reflected photons into the medium but have little effect on deeper propagating photons. More reflective sensors would enable exiting photons to re-enter the tissue and continue propagating in superficial regions – possibly via repeated reflections off the sensor surface – thus increasing detection of shallow-penetrating light. As a result, Oximeter A was likely more sensitive to the properties of superficial layers.

It is also noteworthy that for Oximeter A neonatal and pediatric sensors, the StO_2 value measured in the bulk non-perfused phantom slab was similar to the levels approached as the superficial layer was increased in thickness. This relationship may provide insight into the device's penetration depth and the degree to which displayed values may in many cases represent some weighted version of StO_2 in superficial and deeper layers. The StO_2 values displayed by both oximeters during slab measurements also raise questions about the utility of these devices in low perfusion conditions. The differences in these StO_2 values may be attributable to the use of different algorithms for each device/sensor combination.

These findings align well with prior studies that have addressed the issue of oximeter penetration depth. While we are not aware of any prior phantom study which addressed the impact of superficial layers on cerebral oximetry, Nasseri *et al.* [28] studied how adipose tissue thickness changes estimates of muscle StO_2 using adult probes and a liquid phantom with superficial layers. This study showed an increase in positive bias at lower StO_2 values and greater negative bias at very high StO_2 with superficial layer thickness; trends that are similar to those seen for Oximeter A in Fig. 8. This represents a decrease in sensitivity, in a manner analogous to the effect of decreasing ctHb in cerebral phantoms seen in Kleiser *et al.* [18]. It is also worth noting that Nasseri *et al.* [28] showed minimal impact on accuracy for superficial layer thicknesses less than 5 mm. The greater sensitivity to superficial layer thickness in our study is likely due to a shallower penetration depth of neonatal/pediatric sensors compared to adult sensors. Clinical evidence of reduced oximeter sensitivity with increasing adipose thickness was provided by Wang *et al.* [57], who reported that the change in saturation resulting from an exercise test was shown to decrease as adipose thickness varied from 2.5 to 17 mm.

The results of our phantom measurements with superficial layers also is in good agreement with theoretical work by Okada *et al.* [40]. This study concluded that skull and CSF thickness impact NIRS measurements, with CSF layers causing a shunting effect of photons through the relatively non-scattering subarachnoid space and large layer thicknesses significantly reduce the ability to accurately measure cerebral StO_2. Young *et al.* [58] also found that extra-cerebral regions may create optical channeling of NIR signals from source to detector. These findings are consistent with results in Figs. 8 and 9, which indicate a strong impact of CSF thickness on sensitivity to changes in blood oxygenation. For a CSF layer thickness of 2.5 mm, the neonatal sensor is essentially completely insensitive to changes in the CVM, and the medium sensor is only moderately sensitive to these changes.

4.3 Evaluation of phantom morphology and optical properties

Overall, the 3D printed CVM was shown to provide morphology and optical properties that were sufficiently bio-realistic as to enable testing results that were at least moderately consistent with prior clinical and phantom studies. While the printer has a nominal resolution on the order of 200 μm, the minimum channel size that is printable was much larger, as seen

in Fig. 3. Identifying a suitable channel size involved printing a sample with a range of different channel diameters and using micro-CT imaging to identify the smallest channels that were consistently patent. We previously found that to ensure patency, diameters of approximately 0.8-1 mm were required in biomimetic 3D curved channels [32,33]. This limitation highlights the need for printer quality testing of samples over a range of channel diameters. Resolution limitations of current 3D printers may also complicate development of CVMs for testing oximeters at lower ctHb levels, such as the 25 µM value implemented by Kleiser *et al.* [18] While ideally, the same design would be used with smaller diameter channels, alternate approaches such as dilution of blood may be required to achieve low ctHb levels when such channels cannot be fabricated.

The optical properties provided by the proprietary material are moderately biologically realistic, given the wide range of μ_a and μ_s' values that have been measured in cerebral tissues. One of the complicating factors in identifying a suitable set of optical properties is the irregular morphology of the brain along with the difference in optical properties between white and gray matter regions. Given the limited penetration depth of cerebral NIRS, gray matter is likely the most relevant cerebral tissue; however, light that penetrates this relatively thin (2-5 mm) layer, will encounter white matter which can have scattering coefficients several times higher than gray matter. Another limiting factor for our phantom was the lack of ability to modify the optical properties of the printed material. As a result, the μ_s' in our phantom had a slightly sharper spectral decay than desired, falling from about 11 cm^{-1} at 700 nm to 6 cm^{-1} at 900 nm. Ideally, a more modest decrease from approximately 8 cm^{-1} to 6 cm^{-1} would have been achieved. In future publications, we will explore the use of alternate methods to provide greater flexibility for custom materials that achieve target optical properties.

5. Conclusion

The results of this study provide strong evidence that modular, 3D-printed channel array phantoms are a promising test method for cerebral oximetry. In many cases – particularly those involving thin extracerebral layers – phantom StO_2 measurements collected using clinical devices showed excellent agreement with reference CO-oximeter values. For thicker superficial layers, significant degradation in performance was seen for one of the devices, whereas the other was more robust. Based on comparisons with prior phantom and clinical results, our testing approach provided both absolute quantities and trends that were reasonable. Although improvements in optical property tunability of 3D-printing materials and microchannel print quality will enhance the clinical realism of our approach, this method has the potential to become a powerful tool for elucidating biological factors that impact device performance. Our future work will further validate this approach by testing a greater range of NIRS oximeters and sensors and addressing other confounding biological factors.

Zurich, Switzerland), and Prof. David Busch (UT Southwestern Medical Center, Dallas, Texas, USA).

Disclosures

The mention of commercial products, their sources, or their use in connection with material reported herein is not to be construed as either an actual or implied endorsement of such products by the Department of Health and Human Services, Food and Drug Administration. The authors declare that there are no conflicts of interest related to this article.

References

1. F. van Bel, P. Lemmers, and G. Naulaers, "Monitoring neonatal regional cerebral oxygen saturation in clinical practice: value and pitfalls," Neonatology **94**(4), 237–244 (2008).
2. G. Naulaers, B. Meyns, M. Miserez, V. Leunens, S. Van Huffel, P. Casaer, M. Weindling, and H. Devlieger, "Use of tissue oxygenation index and fractional tissue oxygen extraction as non-invasive parameters for cerebral oxygenation. A validation study in piglets," Neonatology **92**(2), 120–126 (2007).
3. J. J. Volpe, "Brain injury in premature infants: a complex amalgam of destructive and developmental disturbances," Lancet Neurol. **8**(1), 110–124 (2009).
4. M. Wolf, M. Ferrari, and V. Quaresima, "Progress of near-infrared spectroscopy and topography for brain and muscle clinical applications," J. Biomed. Opt. **12**(6), 062104 (2007).
5. F. A. Desmond and S. Namachivayam, "Does near-infrared spectroscopy play a role in paediatric intensive care?" BJA Educ. **16**(8), 281–285 (2016).
6. Y. Yu, K. Zhang, L. Zhang, H. Zong, L. Meng, and R. Han, "Cerebral near-infrared spectroscopy (NIRS) for perioperative monitoring of brain oxygenation in children and adults," Cochrane Database Syst. Rev. **1**, CD010947 (2018).
7. T. J. Germon, N. M. Kane, A. R. Manara, and R. J. Nelson, "Near-infrared spectroscopy in adults: effects of extracranial ischaemia and intracranial hypoxia on estimation of cerebral oxygenation," Br. J. Anaesth. **73**(4), 503–506 (1994).
8. K. T. S. Pattinson, C. H. E. Imray, and A. D. Wright, "What does cerebral oximetry measure?" Br. J. Anaesth. **94**(6), 863–864(2005).
9. L. M. Dix, F. van Bel, W. Baerts, and P. M. Lemmers, "Comparing near-infrared spectroscopy devices and their sensors for monitoring regional cerebral oxygen saturation in the neonate," Pediatr. Res. **74**(5), 557–563 (2013).
10. P. E. Bickler, J. R. Feiner, and M. D. Rollins, "Factors affecting the performance of 5 cerebral oximeters during hypoxia in healthy volunteers," Anesth. Analg. **117**(4), 813–823 (2013).
11. G. Grubhofer, W. Tonninger, P. Keznickl, P. Skyllouriotis 1, M. Ehrlich 1, M. Hiesmayr, and A. Lassnigg, "A comparison of the monitors INVOS 3100 and NIRO 500 in detecting changes in cerebral oxygenation," Acta Anaesthesiol. Scand. **43**(4), 470–475 (1999).
12. A. Pisano, N. Galdieri, T. P. Iovino, M. Angelone, and A. Corcione, "Direct comparison between cerebral oximetry by INVOS(TM) and EQUANOX(TM) during cardiac surgery: a pilot study," Heart Lung Vessel. **6**(3), 197–203 (2014).
13. C. Schmidt, M. Heringlake, P. Kellner, A. E. Berggreen, H. Maurer, S. Brandt, B. Bucsky, M. Petersen, and E. I. Charitos, "The effects of systemic oxygenation on cerebral oxygen saturation and its relationship to mixed venous oxygen saturation: A prospective observational study comparison of the INVOS and ForeSight Elite cerebral oximeters," Can. J. Anaesth. **65**(7), 766–775 (2018).
14. S. N. Davie and H. P. Grocott, "Impact of extracranial contamination on regional cerebral oxygen saturation: a comparison of three cerebral oximetry technologies," Anesthesiology **116**(4), 834–840 (2012).
15. H. Sørensen, N. H. Secher, C. Siebenmann, H. B. Nielsen, M. Kohl-Bareis, C. Lundby, and P. Rasmussen, "Cutaneous vasoconstriction affects near-infrared spectroscopy determined cerebral oxygen saturation during administration of norepinephrine," Anesthesiology **117**(2), 263–270 (2012).
16. A. I. R. Maas and G. Citerio, "Noninvasive monitoring of cerebral oxygenation in traumatic brain injury: a mix of doubts and hope," Intensive Care Med. **36**(8), 1283–1285 (2010).
17. R. N. Kreeger, C. Ramamoorthy, S. C. Nicolson, W. A. Ames, R. Hirsch, L. F. Peng, A. C. Glatz, K. D. Hill, J. Hoffman, J. Tomasson, and C. D. Kurth, "Evaluation of pediatric near-infrared cerebral oximeter for cardiac disease," Ann. Thorac. Surg. **94**(5), 1527–1533 (2012).
18. S. Kleiser, N. Nasseri, B. Andresen, G. Greisen, and M. Wolf, "Comparison of tissue oximeters on a liquid phantom with adjustable optical properties," Biomed. Opt. Express **7**(8), 2973–2992 (2016).
19. C. L. Hunter, J. L. Oei, K. Lui, and T. Schindler, "Cerebral oxygenation as measured by near-infrared spectroscopy in neonatal intensive care: correlation with arterial oxygenation," Acta Paediatr. **106**(7), 1073–1078 (2017).
20. J. Pfefer and A. Agrawal, "A review of consensus test methods for established medical imaging modalities and their implications for optical coherence tomography," Proc. SPIE **8215**, 1–10 (2012).
21. T. Kusaka, K. Isobe, K. Nagano, K. Okubo, S. Yasuda, M. Kondo, S. Itoh, K. Hirao, and S. Onishi, "Quantification of cerebral oxygenation by full-spectrum near-infrared spectroscopy using a two-point method," Comp. Biochem. Physiol. A Mol. Integr. Physiol. **132**(1), 121–132 (2002).

22. F. Martelli, P. Di Ninni, G. Zaccanti, D. Contini, L. Spinelli, A. Torricelli, R. Cubeddu, H. Wabnitz, M. Mazurenka, R. Macdonald, A. Sassaroli, and A. Pifferi, "Phantoms for diffuse optical imaging based on totally absorbing objects, part 2: experimental implementation," J. Biomed. Opt. **19**(7), 076011 (2014).

23. D. Ostojic, S. Kleiser, N. Nasseri, H. Isler, B. Andresen, H. Wabnitz, T. Karen, F. Scholkmann, and M. Wolf, "In vitro comparisons of near-infrared spectroscopy oximeters: impact of slow changes in scattering of liquid phantoms," in *Oxygen Transport to Tissue XL*, O. Thews, J. C. LaManna, and D. K. Harrison, eds. Adv Exp Med Biol (2018), pp 375–379.

24. C. D. Kurth, H. Liu, W. S. Thayer, and B. Chance, "A dynamic phantom brain model for near-infrared spectroscopy," Phys. Med. Biol. **40**(12), 2079–2092 (1995).

25. A. Hussain, W. Petersen, J. Staley, E. Hondebrink, and W. Steenbergen, "Quantitative blood oxygen saturation imaging using combined photoacoustics and acousto-optics," Opt. Lett. **41**(8), 1720–1723 (2016).

26. S. Hyttel-Sorensen, S. Kleiser, M. Wolf, and G. Greisen, "Calibration of a prototype NIRS oximeter against two commercial devices on a blood-lipid phantom," Biomed. Opt. Express **4**(9), 1662–1672 (2013).

27. S. Suzuki, S. Takasaki, T. Ozaki, and Y. Kobayashi, "Tissue oxygenation monitor using NIR spatially resolved spectroscopy," Proc. SPIE **3597**, 582–592 (1999).

28. N. Nasseri, S. Kleiser, D. Ostojic, T. Karen, and M. Wolf, "Quantifying the effect of adipose tissue in muscle oximetry by near infrared spectroscopy," Biomed. Opt. Express **7**(11), 4605–4619 (2016).

29. S. Kleiser, D. Ostojic, B. Andresen, N. Nasseri, H. Isler, F. Scholkmann, T. Karen, G. Greisen, and M. Wolf, "Comparison of tissue oximeters on a liquid phantom with adjustable optical properties: an extension," Biomed. Opt. Express **9**(1), 86–101 (2018).

30. L. Spinelli, M. Botwicz, N. Zolek, M. Kacprzak, D. Milej, P. Sawosz, A. Liebert, U. Weigel, T. Durduran, F. Foschum, A. Kienle, F. Baribeau, S. Leclair, J. P. Bouchard, I. Noiseux, P. Gallant, O. Mermut, A. Farina, A. Pifferi, A. Torricelli, R. Cubeddu, H. C. Ho, M. Mazurenka, H. Wabnitz, K. Klauenberg, O. Bodnar, C. Elster, M. Bénazech-Lavoué, Y. Bérubé-Lauzière, F. Lesage, D. Khoptyar, A. A. Subash, S. Andersson-Engels, P. Di Ninni, F. Martelli, and G. Zaccanti, "Determination of reference values for optical properties of liquid phantoms based on Intralipid and India ink," Biomed. Opt. Express **5**(7), 2037–2053 (2014).

31. J. Wang, J. Coburn, C.-P. Liang, N. Woolsey, J. C. Ramella-Roman, Y. Chen, and T. J. Pfefer, "Three-dimensional printing of tissue phantoms for biophotonic imaging," Opt. Lett. **39**(10), 3010–3013 (2014).

32. P. Ghassemi, J. Wang, A. J. Melchiorri, J. C. Ramella-Roman, S. A. Mathews, J. C. Coburn, B. S. Sorg, Y. Chen, and T. J. Pfefer, "Rapid prototyping of biomimetic vascular phantoms for hyperspectral reflectance imaging," J. Biomed. Opt. **20**(12), 121312 (2015).

33. Y. Liu, P. Ghassemi, A. Depkon, M. I. Iacono, J. Lin, G. Mendoza, J. Wang, Q. Tang, Y. Chen, and T. J. Pfefer, "Biomimetic 3D-printed neurovascular phantoms for near-infrared fluorescence imaging," Biomed. Opt. Express **9**(6), 2810–2824 (2018).

34. B. Z. Bentz, A. G. Bowen, D. Lin, D. Ysselstein, D. H. Huston, J.-C. Rochet, and K. J. Webb, "Printed optics: phantoms for quantitative deep tissue fluorescence imaging," Opt. Lett. **41**(22), 5230–5233 (2016).

35. G. Liu, K. Huang, Q. Jia, S. Liu, S. Shen, J. Li, E. Dong, P. Lemaillet, D. W. Allen, and R. X. Xu, "Fabrication of a multilayer tissue-mimicking phantom with tunable optical properties to simulate vascular oxygenation and perfusion for optical imaging technology," Appl. Opt. **57**(23), 6772–6780 (2018).

36. S. S. Margulies and K. L. Thibault, "Infant skull and suture properties: measurements and implications for mechanisms of pediatric brain injury," J. Biomech. Eng. **122**(4), 364–371 (2000).

37. A. Demel, K. Feilke, M. Wolf, C. F. Poets, and A. R. Franz, "Correlation between skin, bone, and cerebrospinal fluid layer thickness and optical coefficients measured by multidistance frequency-domain near-infrared spectroscopy in term and preterm infants," J. Biomed. Opt. **19**(1), 017004 (2014).

38. C. D. Kurth and W. S. Thayer, "A multiwavelength frequency-domain near-infrared cerebral oximeter," Phys. Med. Biol. **44**(3), 727–740 (1999).

39. L. Giacometti, "Facts, legends, and myths about the scalp throughout history," Arch. Dermatol. **95**(6), 629–631 (1967).

40. E. Okada and D. T. Delpy, "Near-infrared light propagation in an adult head model. I. Modeling of low-level scattering in the cerebrospinal fluid layer," Appl. Opt. **42**(16), 2906–2914 (2003).

41. P. Zee, M. Essenpreis, and D. T. Delpy, "Optical properties of brain tissue," Proc. SPIE **1888**, 454–465 (1993).

42. P. Farzam, E. M. Buckley, P.-Y. Lin, K. Hagan, P. E. Grant, T. E. Inder, S. A. Carp, and M. A. Franceschini, "Shedding light on the neonatal brain: probing cerebral hemodynamics by diffuse optical spectroscopic methods," Sci. Rep. **7**(1), 15786 (2017).

43. S. C. Gebhart, W. C. Lin, and A. Mahadevan-Jansen, "In vitro determination of normal and neoplastic human brain tissue optical properties using inverse adding-doubling," Phys. Med. Biol. **51**(8), 2011–2027 (2006).

44. F. Bevilacqua, D. Piguet, P. Marquet, J. D. Gross, B. J. Tromberg, and C. Depeursinge, "In vivo local determination of tissue optical properties: applications to human brain," Appl. Opt. **38**(22), 4939–4950 (1999).

45. A. Farina, A. Torricelli, I. Bargigia, L. Spinelli, R. Cubeddu, F. Foschum, M. Jäger, E. Simon, O. Fugger, A. Kienle, F. Martelli, P. Di Ninni, G. Zaccanti, D. Milej, P. Sawosz, M. Kacprzak, A. Liebert, and A. Pifferi, "In-vivo multilaboratory investigation of the optical properties of the human head," Biomed. Opt. Express **6**(7), 2609–2623 (2015).

46. S. A. Prahl, "The Adding-Doubling Method," in *Optical-Thermal Response of Laser-Irradiated Tissue*, A. J. Welch and M. J. C. Van Gemert, eds. (Springer US, Boston, MA, 1995), pp. 101–129.

47. S. Ijichi, T. Kusaka, K. Isobe, K. Okubo, K. Kawada, M. Namba, H. Okada, T. Nishida, T. Imai, and S. Itoh, "Developmental changes of optical properties in neonates determined by near-infrared time-resolved spectroscopy," Pediatr. Res. **58**(3), 568–573 (2005).
48. J. Choi, M. Wolf, V. Toronov, U. Wolf, C. Polzonetti, D. Hueber, L. P. Safonova, R. Gupta, A. Michalos, W. Mantulin, and E. Gratton, "Noninvasive determination of the optical properties of adult brain: near-infrared spectroscopy approach," J. Biomed. Opt. **9**(1), 221–229 (2004).
49. W. G. Zijlstra and A. Buursma, "Spectrophotometry of hemoglobin: absorption spectra of bovine oxyhemoglobin, deoxyhemoglobin, carboxyhemoglobin, and methemoglobin," Biochem. Mol. Biol. J. **118**(4), 743–749 (1997).
50. S. J. Barker, K. K. Tremper, and J. Hyatt, "Effects of methemoglobinemia on pulse oximetry and mixed venous oximetry," Anesthesiology **70**(1), 112–117 (1989).
51. ISO 80601, "Medical electrical equipment–Part 2-61: Particular requirements for basic safety and essential performance of pulse oximeter equipment," (2017 updated).
52. S. Hyttel-Sorensen, T. W. Hessel, and G. Greisen, "Peripheral tissue oximetry: comparing three commercial near-infrared spectroscopy oximeters on the forearm," J. Clin. Monit. Comput. **28**(2), 149–155 (2014).
53. A. Schneider, B. Minnich, E. Hofstätter, C. Weisser, E. Hattinger-Jürgenssen, and M. Wald, "Comparison of four near-infrared spectroscopy devices shows that they are only suitable for monitoring cerebral oxygenation trends in preterm infants," Acta Paediatr. **103**(9), 934–938 (2014).
54. T. W. Hessel, S. Hyttel-Sorensen, and G. Greisen, "Cerebral oxygenation after birth - a comparison of INVOS(®) and FORE-SIGHT™ near-infrared spectroscopy oximeters," Acta Paediatr. **103**(5), 488–493 (2014).
55. B. Hallacoglu, A. Sassaroli, and S. Fantini, "Optical characterization of two-layered turbid media for non-invasive, absolute oximetry in cerebral and extracerebral tissue," PLoS One **8**(5), e64095 (2013).
56. M. A. Franceschini, S. Fantini, L. A. Paunescu, J. S. Maier, and E. Gratton, "Influence of a superficial layer in the quantitative spectroscopic study of strongly scattering media," Appl. Opt. **37**(31), 7447–7458 (1998).
57. W. Feng, D. Haishu, T. Fenghua, Z. Jun, X. Qing, and T. Xianwu, "Influence of overlying tissue and probe geometry on the sensitivity of a near-infrared tissue oximeter," Physiol. Meas. **22**(1), 201–208 (2001).
58. A. E. Young, T. J. Germon, N. J. Barnett, A. R. Manara, and R. J. Nelson, "Behaviour of near-infrared light in the adult human head: implications for clinical near-infrared spectroscopy," Br. J. Anaesth. **84**(1), 38–42 (2000).